Available online at www.sciencedirect.com
ScienceDirect
Trans. Nonferrous Met. Soc. China 32(2022) 2510−2526
Transactions of Nonferrous Metals Society of China
www.tnmsc.cn

Effect of yttrium and calcium additions on electrochemical behaviors and discharge performance of AZ80 anodes for Mg−air battery

Yu-wen-xi ZHANG[1], Lu HAN[1], Lin-bao REN[2], Ling-ling FAN[1],
Yang-yang GUO[3], Ming-yang ZHOU[4], Gao-feng QUAN[1]

1. Key Laboratory of Advanced Technologies of Materials (Ministry of Education),
School of Materials Science and Engineering, Southwest Jiaotong University, Chengdu 610031, China;
2. Center for Advancing Materials Performance from the Nanoscale,
State Key Laboratory for Mechanical Behavior of Materials, Xi'an Jiaotong University, Xi'an 710049, China;
3. Xi'an Rare Metal Materials Institute Co., Ltd., Xi'an 710049, China;
4. Science and Technology on Reactor System Design Technology Laboratory,
Nuclear Power Institute of China, Chengdu 610213, China

Received 8 August 2021; accepted 1 April 2022

Abstract: The effects of yttrium (Y) and yttrium + calcium (Y+Ca) additions on the electrochemical properties and discharge performance of the as-extruded Mg−8Al−0.5Zn−0.2Mn (AZ80) anodes for Mg−air batteries were investigated. The results show that the addition of 0.2 wt.% Y increased the corrosion resistance and discharge activity of AZ80 anode. This was attributed to the fine and spherical β-$Mg_{17}Al_{12}$ phases dispersing evenly in AZ80+0.2Y alloy, which suppressed the localized corrosion and severe "chunk effect", and facilitated the rapid activation of α-Mg. Combinative addition of 0.2 wt.% Y and 0.15 wt.% Ca generated grain refinement and a reduction of the β-$Mg_{17}Al_{12}$ phase, resulting in a further enhancement in discharge voltage. However, the incorporation of Ca in $Mg_{17}Al_{12}$ and Al_2Y compounds compromised the corrosion resistance and anodic efficiency of AZ80+0.2Y+0.15Ca anode. Consequently, AZ80+0.2Y anode exhibited excellent overall discharge performance, with the peak discharge capacity and anodic efficiency of 1525 mA·h·g^{-1} and 67% at 80 mA/cm^2, 13% and 14% higher than those of AZ80 anode, respectively.
Key words: Mg−air battery; Mg−Al−Zn anode; discharge performance; electrochemical behavior

1 Introduction

Mg is a promising anode material in the metal−air battery, attributed to its negative standard electrode (SE) potential of −2.37 V vs. standard hydrogen electrode (SHE), which can produce a high Faradic capacity of 2205 mA·h·g^{-1}, behind lithium (−3.04 V (vs SHE) and 3682 mA·h·g^{-1}) [1,2]. Additionally, the neutral saltine electrolyte is adequate for the Mg−air battery due to Mg comparative chemical stabilization in an aqueous solution, while lithium (Li) reacts acutely with water [3]. However, the actual discharge voltage, capacity, and power energy of Mg are lower than the theoretical values due to its severe self-corrosion, negative difference effect, and adherent passive corrosion products film on the surface, impeding the ion transformation and electrochemical reaction between anode and electrolyte [4]. Thus, it is crucial to solving the considerable voltage drop and poor anodic efficiency in the Mg−air battery for its commercial applications.

Corresponding author: Gao-feng QUAN, Tel: +86-13980066985, E-mail: quangf@swjtu.edu.cn
DOI: 10.1016/S1003-6326(22)65962-4

Alloying in Mg has been reported to effectively mitigate the above problems, such as Al, Pb, Zn, Hg, Ga, Li, Ca, Mn, Sn and rare earth (RE). Most of these elements play a role in decelerating corrosion of Mg because of their internal nobler potential and higher overpotential for hydrogen evolution [5]. The purification effect on molten Mg can significantly repress the parasitic corrosion arising from Fe, Ni, Cu, etc. For instance, 0.2 wt.% Mn addition can passivate Fe by forming intermetallic particles Al−Mn−Fe to the melted bottom [6]. Al is a primary alloying element in the Mg alloy systems with a similar low density to enhance the mechanical properties, corrosion resistance, and discharge properties of Mg alloys. Al is generally added with other elements to achieve higher overall performance. Mg−Al−Li alloy is a satisfactory anode material because Li possesses the highest SE potential [2]. Unfortunately, the existing preparation problems and the extreme electrochemical activity of Li-containing alloys distinctly limit the Mg−Al−Li alloy development in metal−air batteries. The Mg−Al−Pb alloy also performs excellent discharge properties, especially at large current density [7−9]. Nevertheless, the anodes containing Pb element cannot be widely applied in the power source for its biological toxicity, the same as that of Hg and Ga elements [10].

Mg−Al−Zn (AZ) alloys, as commercial structural Mg alloys, have attracted a lot of attention to be used as anode materials in Mg batteries, such as AZ31 [11−13], AZ80 [14−16], and AZ91 [17,18]. In comparison, the corrosion rate of AZ80 alloy is relatively low attributed to the higher Al alloying and the continuous network-like distribution of β-$Mg_{17}Al_{12}$, which serves as a barrier to impede the corrosion expansion [19]. With the further rise of Al content (exceeding 8 wt.%), the corrosion potential becomes even nobler, and the discharge activity is greatly weakened [20]. Hence, AZ80 alloy might be the optimal anode material for the relative equilibrium in corrosion rate and kinetics of the electrode reaction. However, the discharge voltage and anodic efficiency of Mg−Al−Zn ternary alloys cannot satisfy the increased demand for Mg−air batteries. Many researchers attempted to further improve the discharge properties of Mg−Al−Zn alloys by alloying with more elements. CHEN et al [15] reported that adding 1−3 wt.% Sm to AZ80 alloy can facilitate the anode discharging since small-sized Al_2Sm particles promote grain refinement, uniform dissolution of the matrix, and easier stripping of discharge products. LIU et al [13,18] studied the influence of multiple alloying with Ca, Sm, and La on the electrochemical behavior of AZ31 and AZ91 alloys, and found that combinative addition of RE elements and Ca is a more effective method to enhance the discharge properties of Mg alloys. Ca is an electrochemically active element with more negative SE potential (−2.87 V vs. SHE) than Mg, which is conducive to improving the discharge activity of Mg and its alloys [21,22]. The grain refinement and the alleviation of hydrogen evolution reaction brought about by the addition of RE elements can effectively restrain the localized corrosion [12].

Y is also an influential RE element in improving the corrosion resistance of Mg alloys. Trace addition of Y (0.5−1 wt.%) in Mg−Li anodes can enhance the cell voltage and power density of Mg−H_2O_2 semi-fuel cells by expediting spalling of corrosion products [23]. WANG et al [24] found that adding 0.2 wt.% Y and 0.2 wt.% Ce into Mg−Al−Pb alloy can refine the microstructure and generate a significant fraction of tiny γ phases (Al_2Ce and Al_2Y), which activates the electrode reaction and promotes anode dissolving uniformly. Nevertheless, the effect of sole Y addition on the discharge performance of Mg−Al−Zn alloy anodes is still unclear. Whether the combined addition of Y and Ca would greatly accelerate the discharge of Mg anodes has not been investigated. Therefore, this work aims to investigate and compare the effects of sole Y addition (0.2 wt.%) and combinative addition of Y and Ca (0.2Y+0.15Ca, wt.%) on the electrochemical behaviors and discharge properties of AZ80 anodes.

2 Experimental

2.1 Materials preparation

AZ80, AZ80+0.2Y, and AZ80+0.2Y+0.15Ca magnesium alloys were served as experimental anode materials in this work. The chemical compositions were measured using an inductively coupled plasma optical emission spectrometer (ICP-OES), and the results are listed in Table 1. The cast ingots were prepared by resistance furnace

Table 1 ICP results for actual chemical composition of investigated alloys (wt.%)

Alloy	Al	Zn	Y	Ca	Mn	Mg
AZ80	8.09	0.94	−	−	0.27	Bal.
AZ80+0.2Y	8.09	0.98	0.21	−	0.11	Bal.
AZ80+0.2Y+0.15Ca	8.03	0.94	0.20	0.15	0.18	Bal.

melting pure Mg (99.95 wt.%), pure Al (99.99 wt.%), pure Zn (99.99 wt.%), Mg−30Y (wt.%), and Mg−20Ca (wt.%) master alloys in a mild-steel crucible. The molten alloys were protected from oxidation by a covering flux and CO_2 + 2 vol.% SF_6 mixed gas. The melt was stirred at 1033 K with a refining agent (JMDJ) to remove impurities and homogenize the alloy composition. Then, the melt was poured into *d*95 mm steel die after holding at 1013 K for 50−60 min, which was preheated at 473 K. The billets were machined into *d*90 mm round bars and homogenized for 8 h at 693 K. In order to make the grain size and second phase as fine and uniform as possible to obtain better corrosion resistance and discharge performance, we employed the extrusion process. The extruded round bars of 16 mm in diameter were gained by hot extrusion at 623 K, with the extrusion ratio and extrusion rate of 32:1 and 0.3 mm/s, respectively. As a result, all specimens had detection sections parallel to the extruding direction (ED).

2.2 Microstructure characterization

The samples were ground with silicon carbide (SiC) papers from 400 to 2000 grits, then polished to a mirror-like finish, and etched using a solution of 5 g picric acid, 5 g acetic acid, 10 mL distilled water and 100 mL ethanol. The microstructure characterization was conducted on the optical microscope (OM) (Zeiss Axio Lab. A1). A linear intercept method was employed to measure the average grain size, and the precipitation area fraction in alloys was measured by Image-Pro Plus 6.0. Scanning electronic microscopy (SEM) image was obtained at a voltage of 2.7 kV in Quanta FEG 250 SEM. The chemical elements analysis was conducted in the X-max^n energy disperse spectrometer (EDS). The phase composition was determined by X-ray diffraction (XRD) in PANalytical X′Pert Pro with Cu $K_{\alpha 1}$ radiation (λ=0.154 nm), and the selected parameters were 30 kV, 50 mA at 298 K with the angle range of 2θ=20°−90° (scan step size 0.033°, time per step 12 s, and continuous scan).

2.3 Electrochemical tests

The electrochemical behavior of investigated alloys was analyzed by open-circuit potentials (OCPs), polarization curves, and electrochemical impedance spectra (EIS), using a classical three electrodes system and 3.5 wt.% NaCl electrolyte. A platinum foil (1 cm^2 surface area) and a saturated calomel electrode (SCE) served as the counter and reference electrodes, respectively. The studied alloys served as the working electrode with an exposed surface of 10 mm × 10 mm, and other areas were sealed with epoxy resin. Before each test, the sample was polished after being ground by 2000 grade SiC papers, degreased by ethanol, cleaned in distilled water and ethanol, and followed by drying in cold flowing air. The OCPs were recorded during 1 h immersion, and polarization curves were obtained with a scan rate of 1 mV/s from cathodic potentials to anodic potentials after 10 min immersion to acquire relatively steady OCPs. Both of them were tested by CorrTest (CS) electrochemistry workstation. The electrochemical impedance spectra (EIS) were measured by the Zahner Zennium electrochemical workstation with the stable value of OCP. The scanned frequency range was from 100 kHz to 0.01 Hz, and the voltage amplitude was 5 mV. Then, the obtained EIS curves were fitted using Zahner analysis software with the acceptable fitting error lower than 5%. All electrochemical measurements were repeated five times, and the results were averaged.

2.4 Corrosion tests

The corrosion rate was examined by hydrogen evolution and mass loss measurement. Specimens were prepared with the same route as electrochemical measurement and immersed in 3.5 wt.% NaCl solution for 58 h at room temperature. The hydrogen gas was collected by a burette above the specimen. Before the test, samples were weighed using an electronic balance (accuracy of ±0.1 mg) to record the initial mass. Moreover, after 58 h immersion, the corroded samples were cleaned by the chromic acid solution (200 g/L CrO_3 + 10 g/L $AgNO_3$) to remove the corrosion products on the surface, flushed by distilled water and ethanol, dried by the cold wind, and then the finial mass was

weighted. The corrosion rate was evaluated according to

$$v=\frac{\Delta m}{s\cdot t} \tag{1}$$

where v is corrosion rate ($mg\cdot cm^{-2}\cdot d^{-1}$); Δm is mass loss (mg); s is surface area (cm^2); t is immersion time (d).

2.5 Mg−air battery tests

The discharge process of AZ80 based anodes for Mg−air battery was monitored using the NEWARE battery testing system. The tested anodic materials with an exposed area of 1 cm^2 were ground with 3000 grade SiC paper and then installed in a homemade Mg−air battery unit, using the MnO_2/C catalyst (Changzhou YOU TE KEI New Energy Technology Co., Ltd.) as the cathode, and 3.5 wt.% NaCl aqueous solution as the electrolyte. The tested area of the air−cathode is 2 mm × 3 mm and 200 mL of electrolyte was added to Mg−air battery device in the test. The discharge curves were recorded at different current densities of 2.5, 5, 10, 20, 40 and 80 mA/cm^2 for 10 h at room temperature (298 K). The anodic efficiency η (%), specific capacity Q ($mA\cdot h\cdot g^{-1}$), and specific energy E ($mW\cdot h\cdot g^{-1}$) were calculated [25]:

$$\eta=\frac{W_{\text{theo}}}{\Delta W}\times 100\% \tag{2}$$

$$W_{\text{theo}}=\frac{I\cdot t_1}{F\cdot\sum\left(\frac{x_i\cdot n_i}{m_i}\right)} \tag{3}$$

$$Q=\frac{I\cdot t_1}{\Delta W}\times 1000 \tag{4}$$

$$E=U\cdot Q \tag{5}$$

where ΔW and W_{theo} represent actual and theoretical mass loss (g) before and after the discharge test, respectively; F is Faraday constant (96485 C/mol); x_i, n_i, and m_i are mass fraction, ionic valence, and molar mass of component i, respectively; I is the impressed discharge current (mA); t_1 is the discharge time (h); U is the discharge voltage (V). The mass loss of the anodes before and after the discharge tests was measured after removing the discharge products using the chromic acid solution. At least three replicates were tested to ensure reliability. In addition, the discharge morphology was examined using SEM.

3 Results and discussion

3.1 Microstructures

Figure 1 shows the SEM micrographs and XRD patterns, together with the corresponding EDS results in Table 2, to analyze the phase composition and distribution of the intermetallic compounds in as-extruded AZ80 based alloys. The irregularly shaped phase in AZ80 alloy (Fig. 1(a)) was mainly β-$Mg_{17}Al_{12}$ (Point A), which was discontinuously distributed around the grain boundaries. There were some additionally oblate particles, identified as Al−Mn phase by EDS analysis (Point B). In Fig. 1(b), β-$Mg_{17}Al_{12}$ phases in AZ80+0.2Y alloy became tinier and rounder, and was dispersed in grain boundaries and interior (Point C). Several large bright white particles (Point D) observed in AZ80+0.2Y alloy were Al_2Y phases, mostly located in trigeminal grain boundaries. With the further addition of Ca, in Fig. 1(c), spherical β-$Mg_{17}Al_{12}$ particles were transformed into slender shapes, and the composition of β-$Mg_{17}Al_{12}$ phase (Point F) incorporated trace Ca about 7.8 wt.% from EDS results. It has been reported by MINGO [6] that Mg_{III} atom of β-$Mg_{17}Al_{12}$ could be replaced by Ca for Ca-containing Mg−Al alloys. Besides, Al_2Y phase containing 14.3 wt.% Y and 23.0 wt.% Ca was detected in AZ80+0.2Y+0.15Ca alloy (Point E), as Al_2(Y,Ca) compound, whose size was smaller than that of Al_2Y phase in AZ80+0.2Y alloy.

It is worth noting that only α-Mg and β-$Mg_{17}Al_{12}$ were identified by XRD in Fig. 1(d), while Al_2Y and Al_2(Y,Ca) compounds were absent in XRD pattern, associated with the low contents of Y and Ca, 0.2 wt.% and 0.15 wt.%, respectively. In addition, the volume fraction of β-$Mg_{17}Al_{12}$ phase was 3.68% in AZ80 alloy, which decreased to 3.17% and 2.92% in AZ80+0.2Y and AZ80+0.2Y+0.15Ca alloys, respectively. The reduction of β-$Mg_{17}Al_{12}$ was ascribed to the preferential formation of Al_2Y and Al_2(Y,Ca) intermetallic compounds, because Al and Y/Ca have a relatively large difference in electronegativity [26,27]. Furthermore, the solid solution of Y increases the solid solution ability of Al [28]. Therefore, a smaller quantity of Al participates in the eutectic reaction ($L\rightarrow\alpha$-Mg + β-$Mg_{17}Al_{12}$) led to a content decrease of β-$Mg_{17}Al_{12}$ phase.

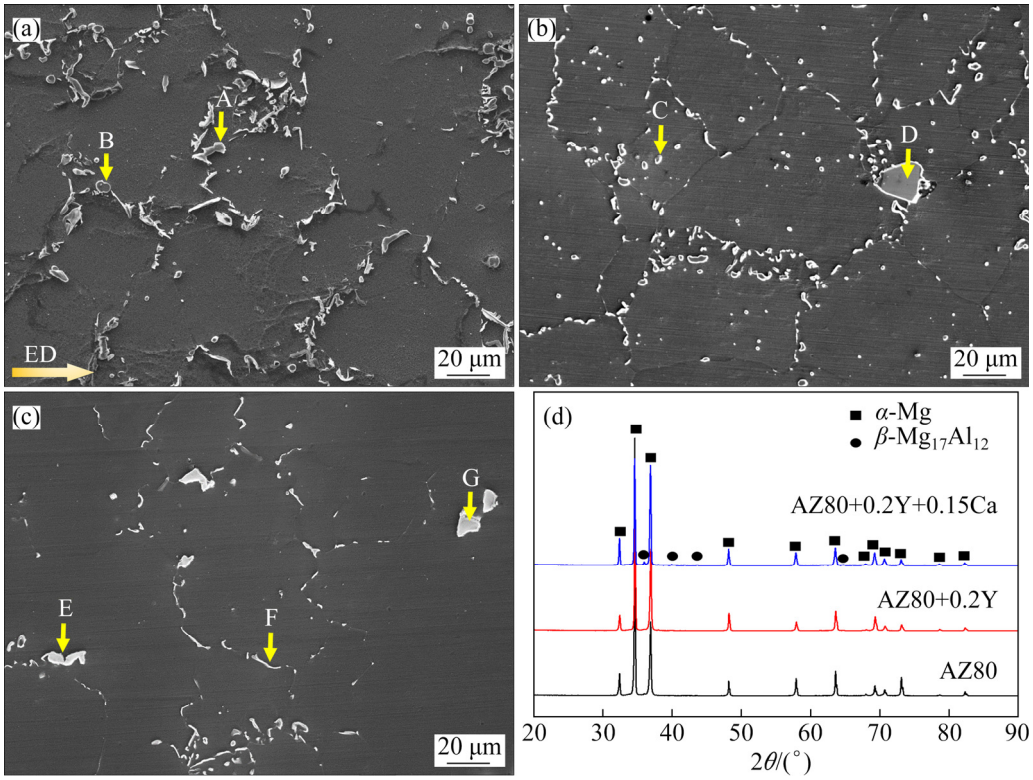

Fig. 1 SEM micrographs for as-extruded AZ80 (a), AZ80+0.2Y (b), AZ80+0.2Y+0.15Ca (c) alloys, and corresponding XRD patterns for studied alloys (d)

Table 2 EDS results of Points A−G in Fig. 1

Point	Content/wt.%					
	Mg	Al	Zn	Mn	Y	Ca
A	58.08	39.28	2.64	–	–	–
B	2.33	53.79	–	43.89	–	–
C	68.01	29.85	2.13	–	–	–
D	3.11	35.90	–	–	60.99	–
E	–	62.60	–	–	14.30	23.0
F	47.70	44.60	–	–		7.80
G	2.70	36.10	–	–	60.90	0.30

Figure 2 depicts the optical microstructure (OM) and grain size distribution of the investigated alloys. Three alloys were all composed of the dynamically recrystallized (DRXed) grains after extrusion, accompanied with the fine second phases along the extrusion direction as the black stripe. There was almost no difference of grain size and distribution between AZ80 and AZ80+0.2Y alloy, while the grain size of AZ80+0.2Y+0.15Ca alloy was 17% smaller than that of AZ80 alloy. The grain refinement effect was derived from the low diffusivity of Ca solute so that the constitutional undercooling appeared in a diffusion layer ahead of the advancing solid/liquid interface [29]. In AZ80 alloy, the gray Al−Mn particles with uniform grain size were observed in OM image. The electric potential difference of Al−Mn phase versus Mg was great, about 380 mV [30], causing strong cathode to accelerate the galvanic corrosion of Mg alloys. In modified AZ80 alloy with 0.2Y and 0.2Y+0.15Ca, however, no such a large amount of Al−Mn phase was found.

3.2 Electrochemical analysis

The open-circuit potentials (OCPs) can reflect the kinetic features without electric current for the electrochemical reaction of alloys. As shown in Fig. 3(a), all OCPs curves of investigated alloys increased rapidly to the peak value in the first 100 s and then decreased to the steady values during the overall 3600 s immersion test in 3.5 wt.% NaCl solution. This phenomenon was attributed to the surface passive film transformation from oxide to thicker hydrated film when exposed to the aqueous solution, along with the film destruction for the existence of Cl^- in the electrolyte [31]. The OCP curves for the micro-alloyed AZ80 alloys remained

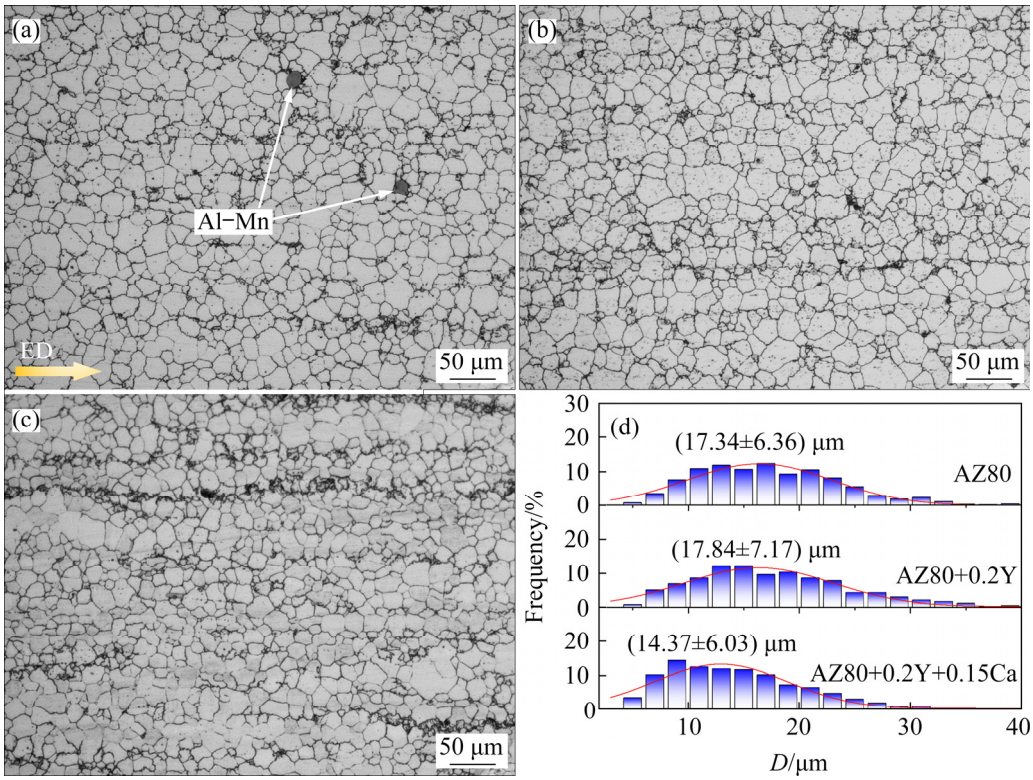

Fig. 2 Optical micrographs of as-extruded AZ80 (a), AZ80+0.2Y (b), AZ80+0.2Y+0.15Ca (c) alloys, and grain size distribution for studied alloys (d)

more negative than those for AZ80 alloy after 1000 s stabilization. Table 3 presents the average potentials (φ_{ocp}) in the steady stage. AZ80+0.2Y+0.15Ca alloy possessed the maximum φ_{ocp} value of −1.612 V (vs SCE), implying the highest electrochemical activity.

The polarization curves of three alloys show a similar tendency in Fig. 3(b), composed of two parts: anodic branch and cathodic branch, referring to the anode oxidation (Eq. (6)) and hydrogen evolution reaction (Eq. (7)) process, respectively:

$$Mg \rightarrow Mg^{2+}+2e \quad (6)$$

$$H_2O+e \rightarrow 1/2H_2+OH^- \quad (7)$$

The inflection points observed in three anodic branches (Fig. 3(b)) were well-connected with the deposition and breakdown of corrosion product $Mg(OH)_2$ film on the anode surface, as a kinetic barrier effect. $Mg(OH)_2$ is slightly soluble in water, which enables the anode surface under protection for a short time, and easily destroyed with increasing current [32]. It can be seen that although the addition of Y and Y+Ca in AZ80 would not change the inner evolution feature of $Mg(OH)_2$ during the polarization process, the combinative addition of Y and Ca decreased the potential of the inflection point to more negative value, suggesting the easier dissolution of $Mg(OH)_2$.

Table 3 lists the electrochemical parameters derived from polarization curves. The corrosion current density, J_{corr}, was evaluated using the Stern–Geary equation [33]:

$$J_{corr}=\frac{\beta_a\beta_c}{2.3R_p(\beta_a-\beta_c)}=\frac{B}{R_p} \quad (8)$$

where β_a is the anodic Tafel slope, β_c is the cathodic Tafel slope of an appropriate polarization curve, and B is a constant involving the Tafel slopes. The corrosion potential (φ_{corr}) indicates a tendency to corrode, while the corrosion rate (v_{corr}) of the anode is proportional to the current density. AZ80+0.2Y+0.15Ca alloy possessed the most negative φ_{corr} of −1.562 V (vs SCE), followed by AZ80+0.2Y and AZ80 alloy, −1.527 and −1.499 V (vs SCE), respectively, which is consistent with the OCP results. The corrosion current density of AZ80+0.2Y alloy was 33.60 μA/cm^2, lower than that of AZ80+0.2Y+0.15Ca, whereas AZ80 alloy had the highest corrosion current density of 48.86 μA/cm^2. Consequently, AZ80+0.2Y alloy

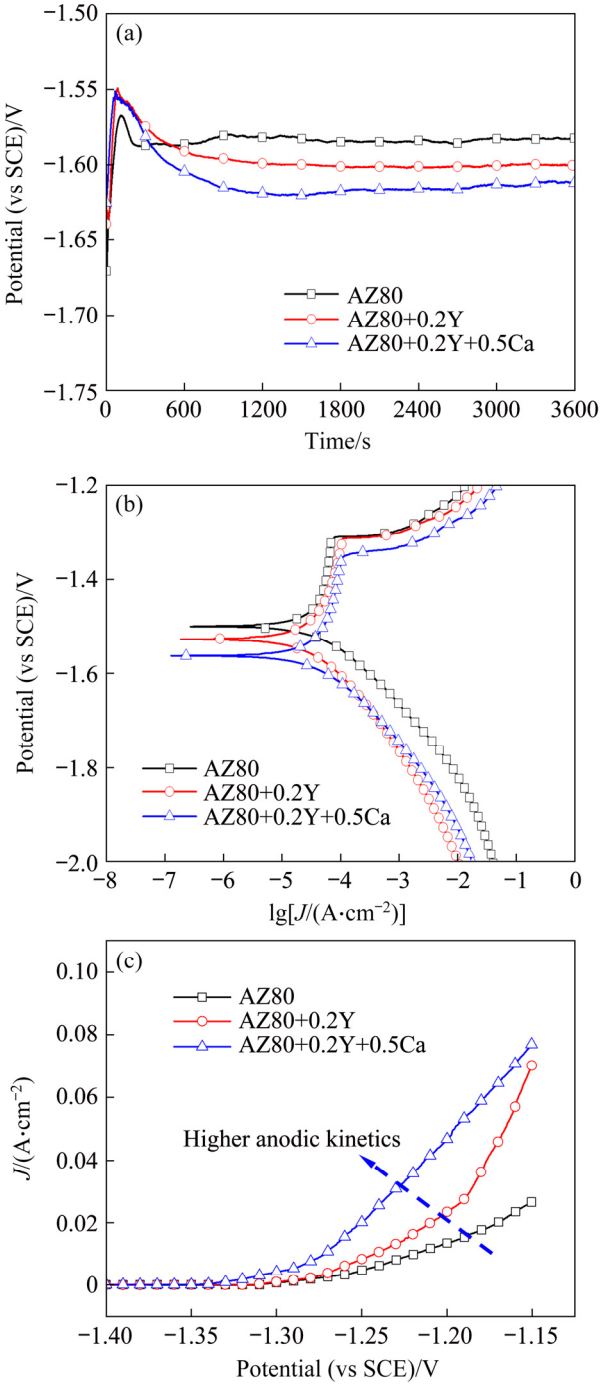

Fig. 3 Electrochemical properties of investigated alloys in 3.5 wt.% NaCl solution: (a) Open circuit potential; (b) Polarization curves; (c) Anodic branches of polarization curves in (b)

displayed the lowest corrosion rate of 0.35 mm/a from the fitting results. The addition of Y into AZ80 alloy could refine, sphere, and disperse β-$Mg_{17}Al_{12}$ phases, which prevents acute localized corrosion. According to the reports of JIA et al [30], the potential difference between α-Mg and β-$Mg_{17}Al_{12}$ would be narrowed by Y alloying by 19−25 mV, thereby weakening the anode polarization. Mg spontaneously dissolving and producing Mg^{2+} ions together with two electrons during the anode polarization process is similar to the Mg anodes consumption in the discharge process of Mg−air battery. Figure 3(c) demonstrates that the anode polarization curves shifted to the higher current density region after adding Y and Ca into AZ80 alloys, indicating an enhancement of anode kinetics. In terms of the above electrochemical analysis, the addition of 0.2Y and 0.2Y+0.15Ca was conducive to boosting the anodic activity and restraining the cathodic kinetics, thus hindering the corrosion rate of AZ80 alloy.

Figure 4 shows the EIS in Nyquist plots and the corresponding equivalent circuit of the investigated alloys under open-circuit conditions. In Fig. 4(a), the Nyquist plot of AZ80 alloy displayed the typical characteristic, agreeing with other studies [14,15], characterized by a high-frequency capacitive loop and a low-frequency inductive loop. The high-frequency capacitive loop represents the charge transfer process at the metal anode/electrolyte interface, where an electric double layer is formed [34]. The corresponding equivalent circuit can be depicted by the parallel connection of charge transfer resistance (R_{ct}) and constant phase elements for the electric double layer (CPE_{dl}). CPE is a non-ideal capacitor associated with the non-homogeneity in the electrochemical system, composed of the magnitude parameter Y and deviation parameter n from 0 (pure resistance) to 1 (pure capacitance). The low-frequency inductive loop is caused by the adsorbed reaction intermediates, implying the ion exchange on the

Table 3 Electrochemical parameters evaluated from OCP and polarization curves

Anode alloy	φ_{ocp}(vs SCE)/V	φ_{corr} (vs SCE)/V	J_{corr}/(μA·cm^{-2})	β_a/(mV·dec^{-1})	β_c/(mV·dec^{-1})	R_p/(Ω·cm^2)	v_{corr}/(mm·a^{-1})
AZ80	−1.584	−1.499	48.86	81.37	188.00	756.23	0.54
AZ80+0.2Y	−1.597	−1.527	33.60	67.10	216.68	1144.62	0.35
AZ80+0.2Y+0.15Ca	−1.612	−1.562	43.91	74.83	202.05	861.57	0.47

naked surface of the Mg anode, which is represented by the inductance (L) and its resistance (R_L) in series [35]. However, for AZ80+0.2Y and AZ80+0.2Y+0.15Ca alloys, the inductive loop disappeared and turned into a capacitive loop at low frequency, which is described by the corrosion products film resistance (R_f) in parallel with CPE_f.

Figures 4(b, c) show the simulated equivalent circuit diagram, and the fitted results are summarized in Table 4. The solution resistance (R_s) is indispensable in equivalent circuits, 5−6 $\Omega\cdot cm^2$ for investigated alloys in the same test system. AZ80 alloy had the lowest R_{ct} (1350 $\Omega\cdot cm^2$) compared with AZ80+0.2Y (3500 $\Omega\cdot cm^2$) and AZ80+0.2Y+0.15Ca (1990 $\Omega\cdot cm^2$) alloys. R_{ct} and R_f correspond to the diameters of the high-frequency and low-frequency loops, respectively, reflecting the corrosion resistance of Mg alloys [36]. AZ80+0.2Y+0.15Ca alloy exhibited the lower R_f, suggesting that more porous and thinner products films are formed on its surface, which is beneficial to maintaining electrochemical reactivity. The sum of R_{ct} and R_f for AZ80+0.2Y alloy was the highest, in agreement with the results of polarization that AZ80+0.2Y alloy possessed the best corrosion resistance. The substitution of inductor for the surface capacitor in AZ80 alloy signifies that its corrosion layer was not as protective as the modified alloys under open-circuit conditions.

The hydrogen evolution and mass loss measurements under the condition of OCPs can be utilized to illustrate the corrosion resistance of investigated alloys in storage; on the other hand, the self-corrosion resistance during discharge can also be predicted by that without applying current [37]. Figure 5(a) demonstrates that the modified alloys were corroded slowly at the initial stage, possibly from the protective oxide/hydroxide film on the surface. With increasing the immersion time, the hydrogen evolution rate increased gradually with the breakdown of protective film, and the volume of hydrogen of AZ80 was larger than that of the other two alloys. The mass loss histogram in Fig. 5(b) also illustrates that AZ80 alloy had a comparatively high corrosion rate of (16.86±2.21) $mg\cdot cm^{-2}\cdot d^{-1}$, while those of AZ80+0.2Y and AZ80+0.2Y+0.15Ca were (5.88±0.17) and (6.46±0.08) $mg\cdot cm^{-2}\cdot d^{-1}$, respectively. Consequently, the micro-alloyed AZ80 alloys exhibited better corrosion resistance than AZ80.

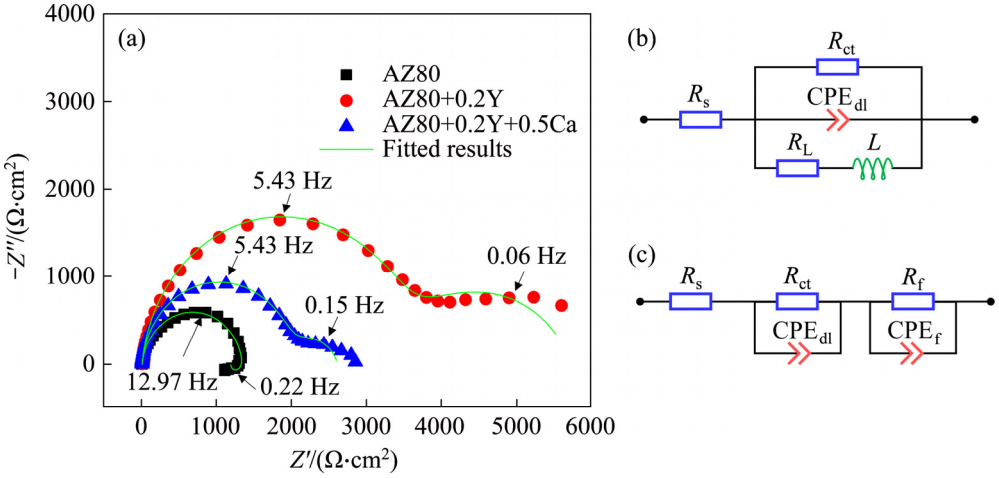

Fig. 4 Electrochemical impedance spectra of investigated alloys in 3.5 wt.% NaCl solution at OCPs: (a) Nyquist plots; (b) Equivalent circuit of AZ80; (c) Equivalent circuit of AZ80+0.2Y and AZ80+0.2Y+0.15Ca

Table 4 Electrochemical parameters of fitted equivalent circuits

Anode alloy	R_s/ ($\Omega\cdot cm^2$)	R_{ct}/ ($\Omega\cdot cm^2$)	Y_{dl}/ ($\Omega^{-1}\cdot cm^{-2}\cdot s^{-1}$)	n_{dl}	R_f/ ($\Omega\cdot cm^2$)	Y_f/ ($\Omega^{-1}\cdot cm^{-2}\cdot s^{-1}$)	n_f	R_L/ ($\Omega\cdot cm^2$)	L/H	Overall error/%
AZ80	5.15	1350	1.14×10^{-5}	0.992	–	–	–	9800	11600	4.92
AZ80+0.2Y	5.84	3500	9.71×10^{-6}	0.942	2230	6.97×10^{-4}	0.751	–	–	2.99
AZ80+0.2Y+0.15Ca	5.77	1990	8.93×10^{-6}	0.945	619	1.08×10^{-3}	0.820	–	–	2.92

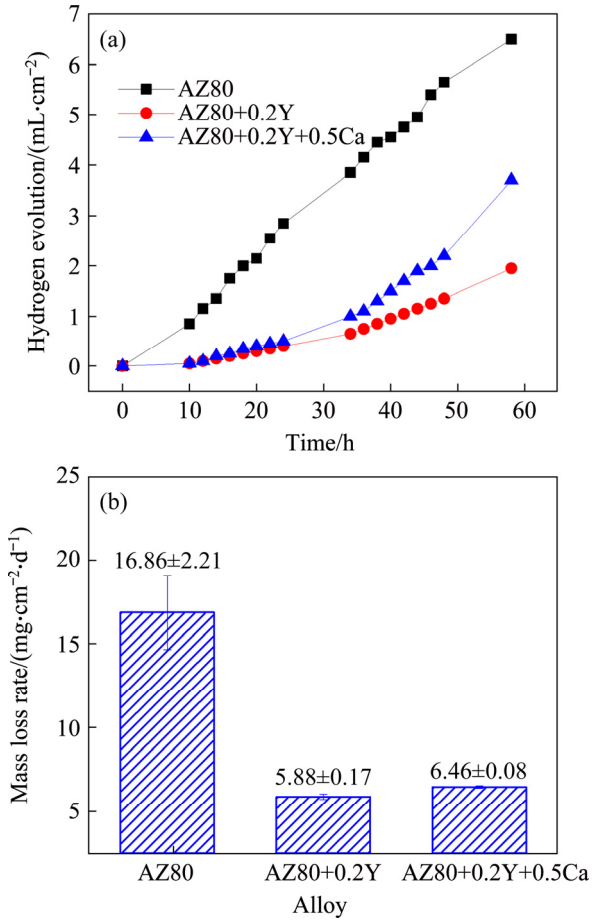

Fig. 5 Hydrogen evolution (a) and mass loss rate (b) of investigated alloys

3.3 Discharge performance of Mg−air batteries

Discharge curves of assembled Mg−air batteries with different anodes in 3.5 wt.% NaCl solution at different current densities from 2.5 to 80 mA/cm^2 are illustrated in Fig. 6. The discharge voltages of modified alloys were higher than those of AZ80 throughout the measuring process, and this superiority expanded with shifting the current density to larger values. AZ80+0.2Y+0.15Ca anode with the highest cell voltage presented the best discharge ability, consistent with the highest electrochemical activity from the results of OCPs and polarization curves. The voltage gradually decayed with the elapsed discharging time and became aggravated as the current density increased. This is ascribed to the augmentation of internal resistance of batteries, electrode polarization, and discharge product covering on anode surface shrinking electrode reaction, etc [38]. When the current density reached 80 mA/cm^2, the discharge curves started to fluctuant with intermittent sawteeth. AZ80 alloy anode presented the most potent voltage drop of about 35 mV/s at 80 mA/cm^2. It can be interpreted by the broken equilibrium in deposition−desorption of surface products where the violent electrode reaction boosts depositing rate, but the detaching rate remains unchanged. The $Mg(OH)_2$ products covering on the surface impeded the electrolyte contacting with Mg anode, leading to dramatic voltage loss during discharge and substantial fluctuation with peeling-off of $Mg(OH)_2$. Adding Y or Y+Ca in AZ80 alloy improved the discharge potential owing to the structure optimization and adjustment of the second phase.

In addition to the cell voltage, the anodic efficiency, specific capacity, and energy density are the critical judging criteria for assembled Mg−air batteries, as-summarized in Fig. 7. According to the computational formula (Eqs. (2)−(5)), the anodic efficiency and specific capacity are both dependent on the mass loss before and after discharge once the discharge current density and duration are determined. As applied current density increases, the mass loss caused by the self-corrosion will decrease due to the inhibited negative difference effect, and the anodic efficiency together with specific capacity will be compromised. The specific energy density, as a product of voltage and specific capacity, demonstrates an overall downward trend together with the cell voltage, indicating that the applied current density has a greater impact on the cell voltage than on the anodic efficiency. In other words, the slight increase in anodic efficiency could not compensate for the loss in cell voltage drop with the increase of the current density.

In summary, AZ80+0.2Y+0.15Ca anode possessed the highest discharge voltage, while AZ80+0.2Y anode performed the supreme anodic efficiency, specific capacity, and energy density. The tiny and uniform β-$Mg_{17}Al_{12}$ globular particles in AZ80+0.2Y alloy are beneficial to discharge activation as well as uniform dissolution. And the refined microstructure of AZ80+0.2Y+0.15Ca alloy is conducive to expediting the electrode reaction kinetics since the augment of grain boundaries can improve atomic diffusion rate and electron activity during the discharge process [39]. Table 5 lists the precise parameters of these three anodes after discharging at 10 mA/cm^2 for 10 h for comparison. All of the anodic efficiencies investigated are less than 60% at 10 mA/cm^2, in which AZ80 possessed

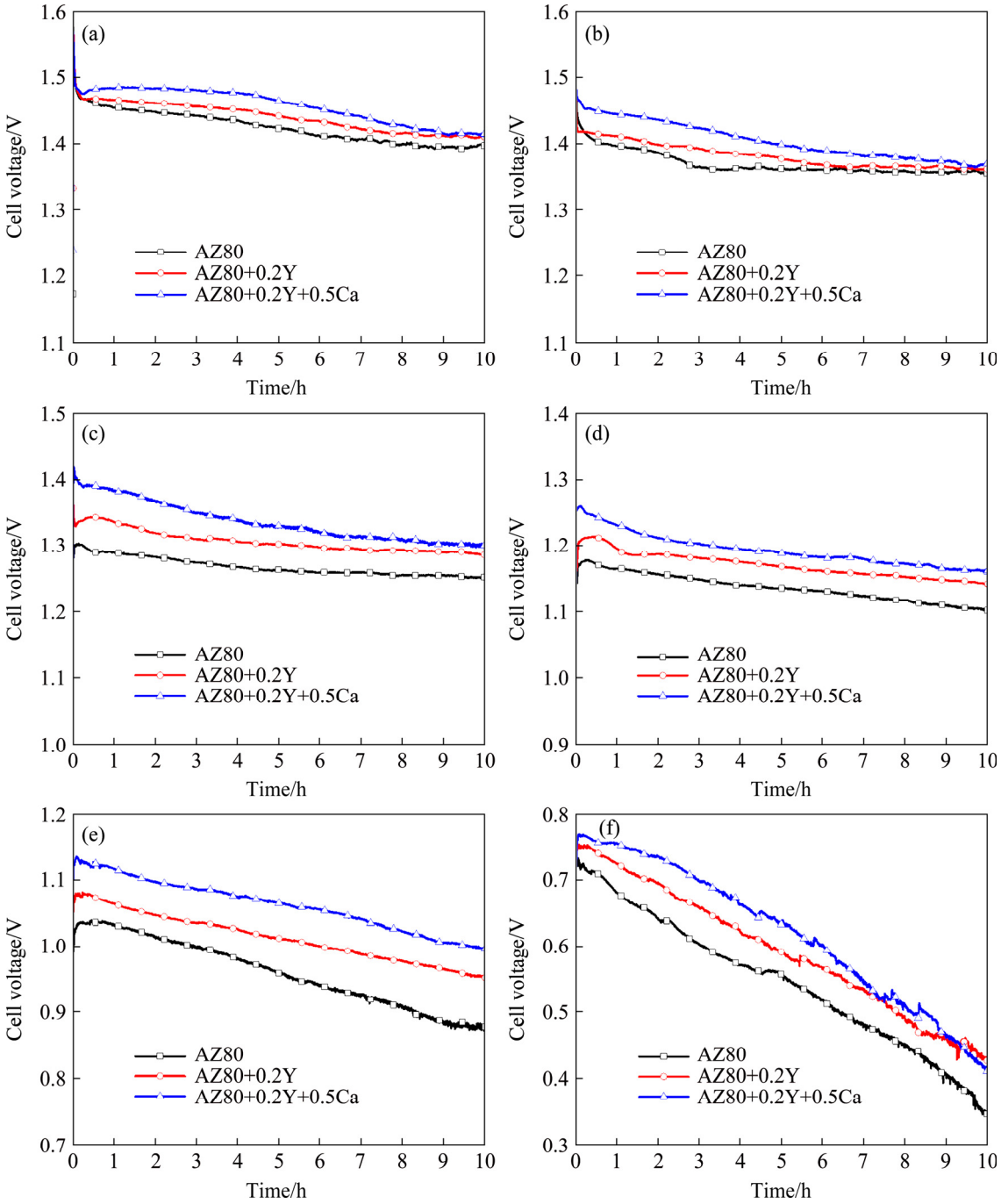

Fig. 6 Discharge curves of investigated anodes in 3.5 wt.% NaCl solution at different current densities: (a) 2.5 mA/cm^2; (b) 5 mA/cm^2; (c) 10 mA/cm^2; (d) 20 mA/cm^2; (e) 40 mA/cm^2; (f) 80 mA/cm^2

the lowest anodic efficiency of 48.55%. The unsatisfactory discharge properties of the AZ80 anode at all current densities were associated with abundant β-$Mg_{17}Al_{12}$ phases and coarse Al−Mn phases. At 80 mA/cm^2, AZ80+0.2Y anode realized the peak anodic efficiency (67%) and specific capacity (1524 mA·h·g^{-1}), which also displayed the highest specific energy density (1671 mW·h·g^{-1}) at 5 mA/cm^2 due to the obvious reduction of discharge voltage at a large current density.

It is worth noting that the cell voltage of AZ80+0.2Y+0.15Ca anode was the highest at different current densities, but the anodic efficiency and specific capacity were lower than those of AZ80+0.2Y anode. On the one hand, alloying Mg with the electrochemically active element Ca could activate the alloy and improve its discharging voltage. On the other hand, Ca incorporated in the

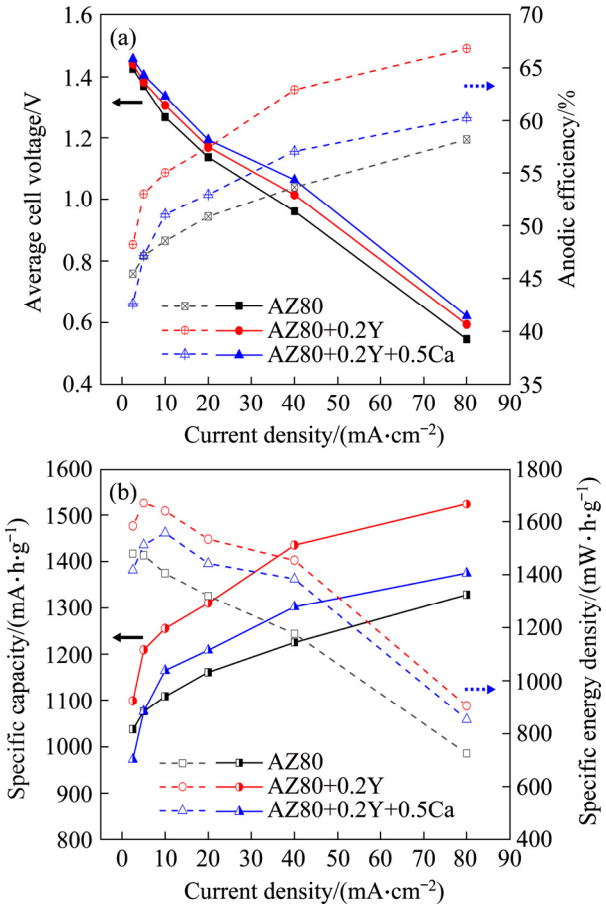

Fig. 7 Discharge properties of assembled Mg−air batteries with different anodes: (a) Average cell voltage and anodic efficiency; (b) Discharge capacity and specific energy

Table 5 Discharge parameters of investigated anodes at 10 mA/cm^2 for 10 h

Alloy	Average voltage/V	Anodic efficiency/%
AZ80	1.268	48.55
AZ80+0.2Y	1.306	55.03
AZ80+0.2Y+0.15Ca	1.337	51.06

Alloy	Specific capacity/(mA·h·g^{-1})	Specific energy density/(mW·h·g^{-1})
AZ80	1109	1405
AZ80+0.2Y	1255	1640
AZ80+0.2Y+0.15Ca	1165	1557

β-$Mg_{17}Al_{12}$ phase could increase the Volta potential difference between β-$Mg_{17}Al_{12}$ and α-Mg [40]; although the increase is slight, it is still deleterious to corrosion resistance. Besides, the Al_2Ca phase is a relatively strong galvanic cathode phase [41]. When Al_2Ca is combined with the Al_2Y phase to form Al_2(Y,Ca) intermetallics, the micro-couple corrosion might be enhanced. Furthermore, the grain refinement from Ca alloying, where more grain boundaries are attacked preferentially during the discharge and corrosion process, can enhance the discharge activity and corrosion rate simultaneously. Accordingly, AZ80+0.2Y anode with excellent overall discharge performance has the great potential for battery anode material.

3.4 Surface morphologies after discharge

To further understand the various discharge performances, the surface morphology of three anodes after discharge is taken into account. Figure 8 displays the surface morphologies before the removal of reaction products after discharging at 2.5 and 10 mA/cm^2 for 10 h. The surface products of Mg anode in the aqueous electrolyte are generated by discharge reaction (Eq. (9)) and self-corrosion reaction (Eq. (10)) synchronously:

$$Mg+1/2O_2+H_2O\rightarrow Mg(OH)_2 \quad (9)$$

$$Mg+2H_2O\rightarrow Mg(OH)_2+H_2 \quad (10)$$

The structure of products $Mg(OH)_2$ is loose and porous, which cannot provide corrosion protection, but hinder the direct contact between the electrolyte and Mg matrix. It can be seen that the AZ80 anode surface was covered by dense and integrated discharge products both at 2.5 and 10 mA/cm^2 in Figs. 8(a, b). In comparison, there were more obvious cracks exiting in the AZ80+0.2Y anode surface in Figs. 8(c, d), and some products were spalled from the substrate in the magnified figure of Fig. 8(c). This phenomenon illustrates that the sole addition of 0.2 wt.% Y in AZ80 anode can promote the breaking up and exfoliation of discharge products, leading to a sufficient discharge reaction. Additionally, the refined and homogeneously-dispersed β-$Mg_{17}Al_{12}$ phases in AZ80+0.2Y anode contributed to the uniform dissolution of the Mg matrix, accompanied by the products being apt to be peeled off. Interestingly, for AZ80+0.2Y+0.15Ca anode, some micron holes on the surface were observed in Fig. 8(e). The inner wall of the hole is smooth and inverted horn-shaped, suggesting these holes are possibly hydrogen stomata. Although the fraction of β-$Mg_{17}Al_{12}$ was reduced after the addition of Y and

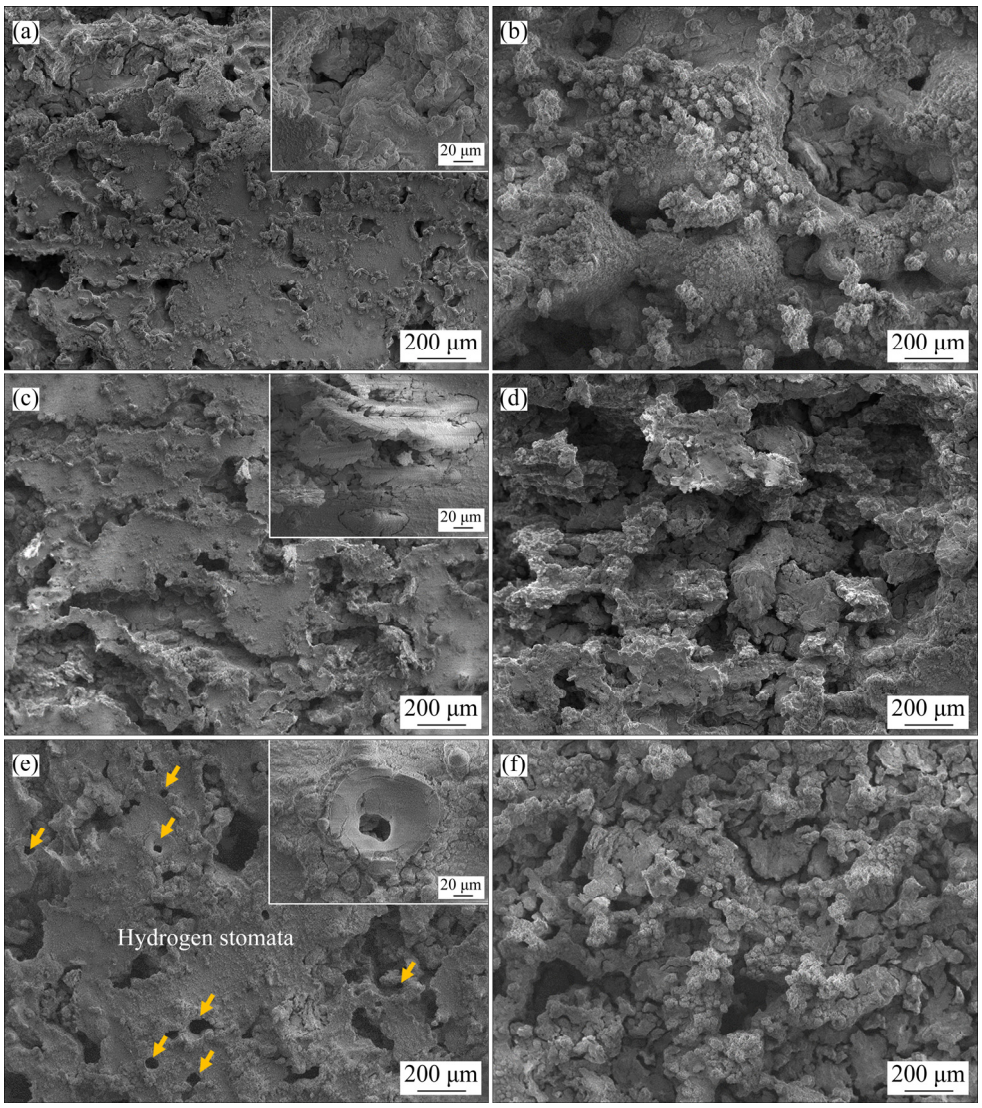

Fig. 8 Surface morphologies with discharge products of AZ80 (a, b), AZ80+0.2Y (c, d) and AZ80+0.2Y+0.15Ca (e, f) anodes after discharge in 3.5 wt.% NaCl solution at 2.5 mA/cm^2 (a, c, e) and 10 mA/cm^2 (b, d, f) for 10 h

Ca, the incorporation of Ca in β-$Mg_{17}Al_{12}$ and Al_2Y phase boosted the partial corrosion reaction. As a result, the enhanced hydrogen evolution destroyed the integrality of corrosion products and attracted the electrolyte to the surface of the fresh Mg matrix through the stomata channel to maintain the discharge reaction. Moreover, in Fig. 8(f), the surface of AZ80+0.2Y+0.15Ca anode shows rising micro-cracks after a discharge process at 10 mA/cm^2 so that the electrolyte can smoothly penetrate the discharge products and react with the Mg substrate.

After removing the discharge products, all of the anodes displayed the island structure, consisting of slightly dissolved flat zones and seriously dissolved depleted zones, as seen in Figs. 9(b, e, h) and 9(c, f, i), respectively. AZ80 anode showed the extremely uneven morphology in Fig. 9(a), and the flat zone was almost free of dissolution in Fig. 9(b), characterized by a few shallow micro-cracks (marked by red arrows) in the matrix and lamellar β-$Mg_{17}Al_{12}$ (marked by white arrows) along the grain boundaries. The depleted zone exhibited the distinctly rugged morphology in Fig. 9(c), where some metal blocks were about to split off around the edge, namely "chunk effect" [42]. This "chunk effect" is ascribed to the abundant discontinued β-$Mg_{17}Al_{12}$ phases agglomerated in the grain boundaries, boosting the dissolution of the surrounding Mg matrix along the grain boundaries. Once the consumption of α-Mg is complete along the boundaries, the undissolved

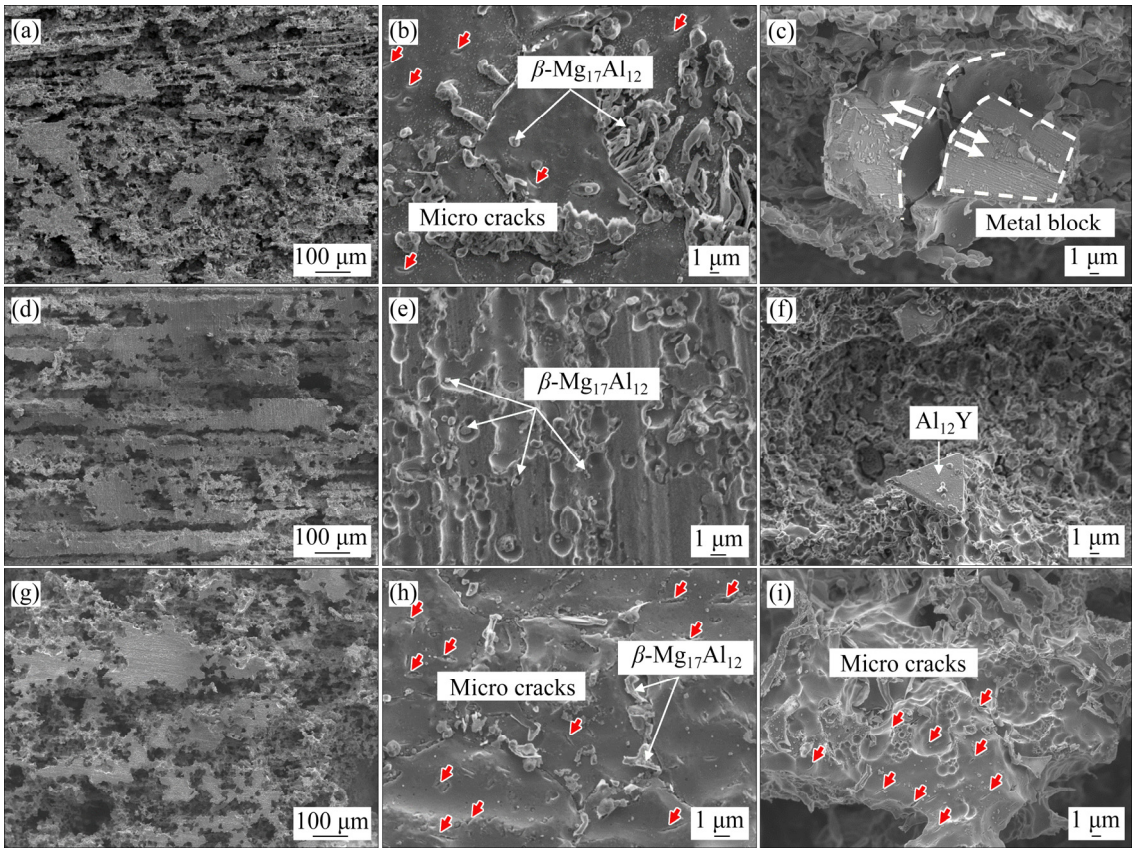

Fig. 9 Surface morphologies after removal of discharge products of AZ80 (a−c), AZ80+0.2Y (d−f), and AZ80+0.2Y+0.15Ca (g−i) anodes after discharge in 3.5 wt.% NaCl solution at 2.5 mA/cm^2 for 10 h

metal blocks entrapped in the discharge products will detach from the surface to the electrolyte and cannot contribute to effective discharge reaction. The Al−Mn phases in AZ80 alloy accelerating the severe accumulated corrosion of Mg matrix is another reason for the decrease of AZ80 discharge efficiency.

In the flat zone of AZ80+0.2Y anode, some fine β-$Mg_{17}Al_{12}$ particles were observed in the etched pits in Fig. 9(e) where α-Mg around these particles was consumed partially. As the dissolution proceeds, the fine β-$Mg_{17}Al_{12}$ particles will fall off easily without the support of the Mg matrix, thus activating Mg dissolution and impeding the severe partial corrosion. The integrated Al_2Y particle remained on the knap of the dissipative matrix after severe dissolution in Fig. 9(f), suggesting that Al_2Y is more electrochemically stable than β-$Mg_{17}Al_{12}$ and cannot bring grievous parasitic corrosion, similar to Ref. [24]. Figures 9(g−i) demonstrate that AZ80+0.2Y+0.15Ca alloy experienced more evident dissolution compared with only 0.2 wt.% Y-modified alloy, which is related to the enhancement of electrochemical activity after Ca addition. However, the substrate of Ca-containing alloy was etched evenly by sodium chloride solution at 2.5 mA/cm^2 in Figs. 9(h, i). In addition, many micro-cracks emerged in the dissolved surface, which is favorable for improving the electrochemical reaction area with electrolytes.

According to Fig. 10, all anodes presented the heavily rugged discharge morphologies at larger current densities of 10 mA/cm^2 after removing the discharge products. There were substantial deep cavities and nearly no undissolved area on the test surface. The magnified images of Figs. 10(b, d, f) illustrated relatively uniform dissolution behavior compared with 2.5 mA/cm^2, attributed to the escalating dissolution rate of the anode with the increase of current density. In addition to several large holes in the AZ80 anode (Fig. 10(a)), some geometrically irregular holes were also observed in dissolution ruins marked by green arrows in Fig. 10(b), which is caused by the mechanical desquamation of metallic particles as “chunk effect”. However, AZ80+0.2Y and AZ80+0.2Y+

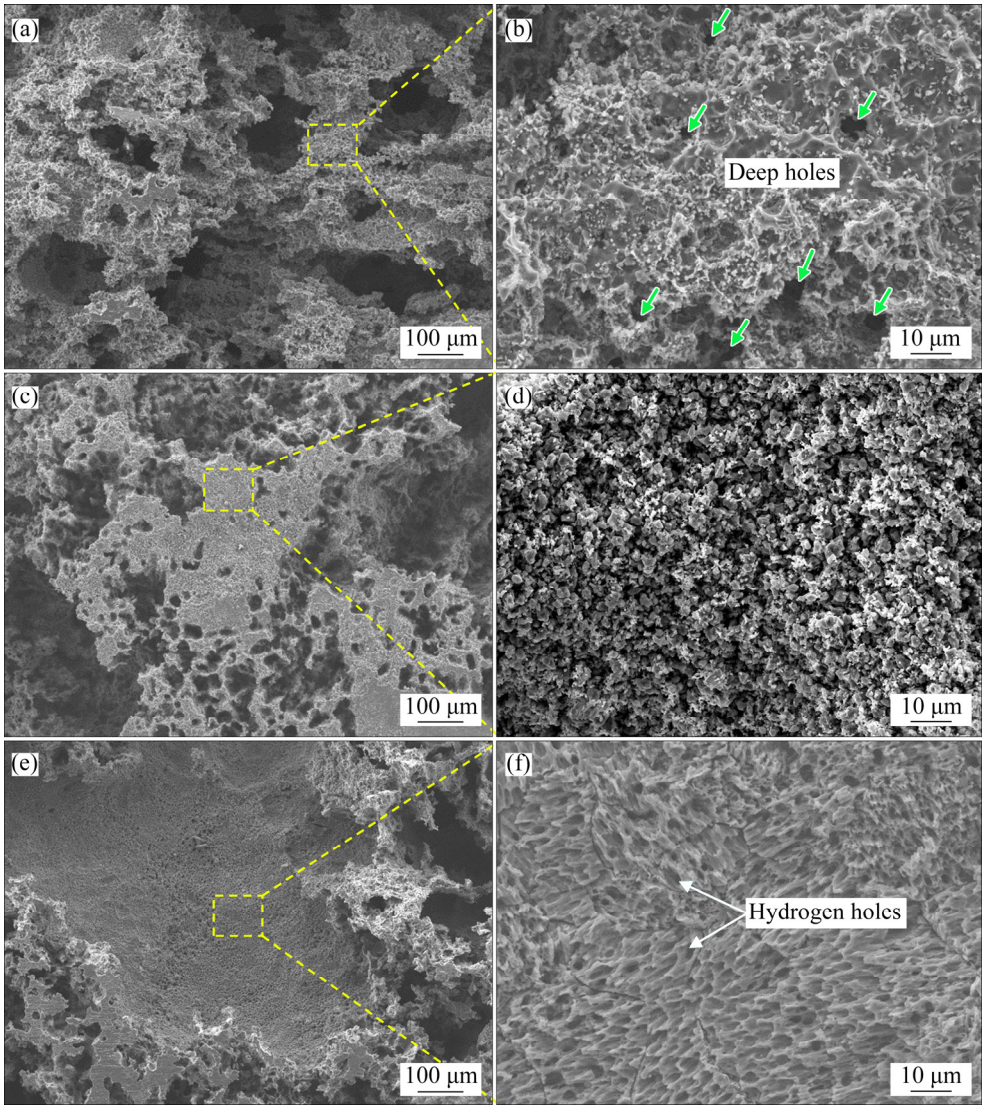

Fig. 10 Surface morphologies after removal of discharge products of AZ80 (a, b), AZ80+0.2Y (c, d), and AZ80+0.2Y+0.15Ca (e, f) anodes after discharge in 3.5 wt.% NaCl solution at 10 mA/cm^2 for 10 h

0.15Ca alloys demonstrated the smoother magnified morphologies, implying more even dissolution for modified anodes. The surface morphology of Ca-containing alloy was featured with dense tiny hydrogen holes after discharging at 10 mA/cm^2 for 10 h in Fig. 10(f), which is different from the large and sparse hydrogen holes on the surface with discharge products at 2.5 mA/cm^2. Although hydrogen evolved from the self-corrosion reaction is deleterious to the anodic efficiency, the released hydrogen can accelerate the rupture and spalling of discharge product to maintain anode interacting with electrolyte.

To clarify the impact of the chunk effect on different anodes, the backscattered electron (BSE) images of the cross-section are presented in Fig. 11. AZ80, AZ80+0.2Y, and AZ80+0.2Y+0.15Ca anodes all experienced severe dissolution during 10 h discharge at 10 mA/cm^2. The test surfaces of three anodes were covered by thick discharge products, in which some undissolved matrix could be seen, surrounded by discharge products and lost the contact with the bulk matrix, a typical chunk effect to destroy the anode utilization. Apart from the abundance of undissolved metallic portions, in AZ80 alloy, extra dissolution pits in the matrix indicated that more serious partial dissolution took place on the other side, gradually developing into chunk effect, as shown in Fig. 9(c). According to Figs. 11(b, c), more homogeneous dissolution and reduced metallic particles were found in micro-alloyed anodes, implying the weakened chunk

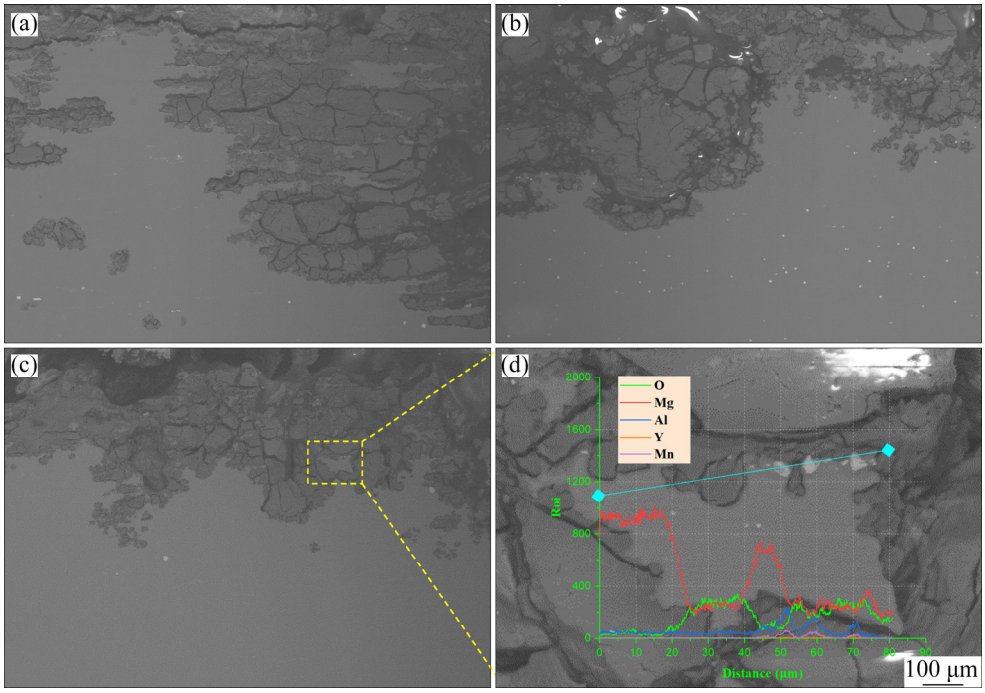

Fig. 11 Cross-sectional morphologies of AZ80 (a), AZ80+0.2Y (b), and AZ80+0.2Y+0.15Ca (c, d) anodes after discharge in 3.5 wt.% NaCl solution at 10 mA/cm^2 for 10 h

effect. In Fig. 11(d), the magnified morphology with EDS line scanning curves suggests that the precipitation of the Al−Mn phase caused a partial chunk effect, which played a considerable role in utilization efficiency loss. Hence, the strong cathodic phase should be circumvented in anode materials design.

4 Conclusions

(1) The sole addition of 0.2 wt.% Y into AZ80 alloy significantly refined and sphered the β-$Mg_{17}Al_{12}$ phase, which dispersed more uniformly in the matrix. The combinative addition of 0.2 wt.% Y and 0.15 wt.% Ca brought 17% grain refinement and reduced the fraction of the β-$Mg_{17}Al_{12}$ phase from 3.68% to 2.92%. Ca participated in the $Mg_{17}Al_{12}$ and Al_2Y phase to replace partial Mg and Y atoms in phase composition, respectively.

(2) The refined, spherical, and reduced β-$Mg_{17}Al_{12}$ phase in modified alloys inhibited the severe localized corrosion, and stimulated a more even electrochemical reaction, resulting in an alleviated chunk effect and enhanced anode utilization. AZ80+0.2Y+0.15Ca alloy possessed the highest electrochemical activity owing to the activation and grain refinement from Ca, but its corrosion resistance was inferior to AZ80+0.2Y alloy since the incorporation of Ca in $Mg_{17}Al_{12}$ and Al_2Y compounds accelerated the galvanic corrosion.

(3) In the Mg−air battery test, AZ80+0.2Y+0.15Ca anode exhibited the highest discharge voltage at all current densities. The plentiful hydrogen evolution in AZ80+0.2Y+0.15Ca anode promoted the $Mg(OH)_2$ products desorption, which was beneficial to improving the reaction activity, but compromised the anodic efficiency. AZ80+0.2Y anode provided peak specific capacity (1524 mA·h·g^{-1}) and anodic efficiency (67%) at 80 mA/cm^2, 13%, and 14% higher than those of AZ80 anode, respectively.

Acknowledgments

The authors acknowledge the financial supports from the Key Development Project of Sichuan Province, China (No. 2017GZ0399), the National Natural Science Foundation of China (No. 52061040), and the Open Projects of the Key Laboratory of Advanced Technologies of Materials, Ministry of Education, Southwest Jiaotong University, China (No. KLATM202003). Acknowledgments are also given to technical support from Litmat Technology Chengdu Co., Ltd., (China).

References

[1] REDDY T B, LINDEN D. Linden's handbook of batteries [M]. 4th ed. New York: McGraw-Hill, 2010.

[2] WANG Nai-guang, WANG Ri-chu, PENG Chao-qun, HU Cheng-wang, FENG Yan, PENG Bing. Research progress of magnesium anodes and their applications in chemical power sources [J]. Transactions of Nonferrous Metals Society of China, 2014, 24: 2427−2439.

[3] CHEN L D, NØRSKOV J K, LUNTZ A C. Theoretical limits to the anode potential in aqueous Mg−air batteries [J]. The Journal of Physical Chemistry C, 2015, 119: 19660−19667.

[4] CHEN Xing-rui, LIU Xuan, LE Qi-chi, ZHANG Ming-xing, LIU Ming, ATRENS A. A comprehensive review of the development of magnesium anodes for primary batteries [J]. Journal of Materials Chemistry A, 2021, 9: 12367−12399.

[5] ESMAILY M, SVENSSON J E, FAJARDO S, BIRBILIS N, FRANKEL G S, VIRTANEN S, ARRABAL R, THOMAS S, JOHANSSON L G. Fundamentals and advances in magnesium alloy corrosion [J]. Progress in Materials Science, 2017, 89: 92−193.

[6] MINGO B, ARRABAL R, MOHEDANO M, MENDIS C L, OLMO R D, MATYKINA E, HORT N, MERINO M C, PARDO A. Corrosion of Mg−9Al alloy with minor alloying elements (Mn, Nd, Ca, Y and Sn) [J]. Materials & Design, 2017, 130: 48−58.

[7] WANG Nai-guang, WANG Ri-chu, PENG Chao-qun, FENG Yan, ZHANG Xiang-yu. Influence of aluminium and lead on activation of magnesium as anode [J]. Transactions of Nonferrous Metals Society of China, 2010, 20: 1403−1411.

[8] DENG Min, WANG Ri-chu, FENG Yan, WANG Nai-guang, WANG Lin-qian. Corrosion and discharge performance of Mg−9%Al−2.5%Pb alloy as anode for seawater activated battery [J]. Transactions of Nonferrous Metals Society of China, 2016, 26: 2144−2151.

[9] FENG Yan, LEI Ge, HE Yu-qing, WANG Ri-chu, WANG Xiao-feng. Discharge performance of Mg−Al−Pb−La anode for Mg−air battery [J]. Transactions of Nonferrous Metals Society of China, 2018, 28: 2274−2286.

[10] WU Jun-liang, WANG Ri-chu, FENG Yan, PENG Chao-qun. Effect of hot rolling on the microstructure and discharge properties of Mg−1.6wt.%Hg−2wt.%Ga alloy anodes [J]. Journal of Alloys and Compounds, 2018, 765: 736−746.

[11] WANG Nai-guang, HUANG Yi-xiang, LIU Jing-jing, YANG Xu-sheng, XIE Wei-peng, CAI Qiong, ZHENG Song-yuan, SHI Zhi-cong. AZ31 magnesium alloy with ultrafine grains as the anode for Mg−air battery [J]. Electrochimca Acta, 2021, 378: 138135.

[12] LIU Xuan, XUE Ji-lai. The role of Al2Gd cuboids in the discharge performance and electrochemical behaviors of AZ31−Gd anode for Mg−air batteries [J]. Energy, 2019, 189: 116314.

[13] LIU Xuan, GUO Zhi-chao, XUE Ji-lai, ZHANG Peng-ju. The role of Al_2Ca and Al_2(Sm,Ca,La) particles in the microstructures and electrochemical discharge performance of as-extruded Mg−3wt.%Al−1wt.%Zn-based alloys for primary Mg−air batteries [J]. International Journal of Energy Research, 2019, 43: 4569−4579.

[14] CHEN Xing-rui, JIA Yong-hui, LE Qi-chi, WANG He-nan, ZHOU Xiong, YU Fu-xiao, ATRENS A. Discharge properties and electrochemical behaviors of AZ80−La−Gd magnesium anode for Mg-air battery [J]. Journal of Magnesium and Alloys, 2020, 9: 2113−2121.

[15] CHEN Xing-rui, LIAO Qi-yu, LE Qi-chi, ZOU Qi, WANG He-nan, ATRENS A. The influence of samarium (Sm) on the discharge and electrochemical behaviors of the magnesium alloy AZ80 as an anode for the Mg−air battery [J]. Electrochimca Acta, 2020, 348: 136315.

[16] CHEN Xing-rui, NING Shao-chen, LE Qi-chi, WANG He-nan, ZOU Qi, GUO Rui-zhen, HOU Jian, JIA Yong-hui, ATRENS A, YU Fu-xiao. Effects of external field treatment on the electrochemical behaviors and discharge performance of AZ80 anodes for Mg−air batteries [J]. Journal of Materials Science & Technology, 2020, 38: 47−55.

[17] XIAO Bo, SONG Guang-Ling, ZHENG Da-jiang, CAO Fu-yong. A corrosion resistant die-cast Mg−9Al−1Zn anode with superior discharge performance for Mg−air battery [J]. Materials & Design, 2020, 194: 108931.

[18] LIU Xuan, XUE Ji-lai, ZHANG Peng-ju, WANG Zeng-jie. Effects of the combinative Ca, Sm and La additions on the electrochemical behaviors and discharge performance of the as-extruded AZ91 anodes for Mg−air batteries [J]. Journal of Power Sources, 2019, 414: 174−182.

[19] PARDO A, MERINO M C, COY A E, VIEJO F, ARRABAL R, FELIÚ Jr S. Influence of microstructure and composition on the corrosion behaviour of Mg/Al alloys in chloride media [J]. Electrochimca Acta, 2008, 53: 7890−7902.

[20] GRIMM, M, LOHMÜLLER A, SINGER R F, VIRTANEN S. Influence of the microstructure on the corrosion behaviour of cast Mg−Al alloys [J]. Corrosion Science, 2019, 155: 95−208.

[21] DENG Min, HÖCHE D, LAMAKA S V, SNIHIROVA D, ZHELUDKEVICH M L. Mg−Ca binary alloys as anodes for primary Mg−air batteries [J]. Journal of Power Sources, 2018, 396: 109−118.

[22] NAKATSUGAWA I, CHINO Y. Discharge performance of Mg−6wt.%Al alloy anodes containing Ca and Zn for magnesium−air batteries [J]. Journal of the Electrochemical Society, 2021, 168: 50507.

[23] LV Yan-zhuo, LIU Min, XU Yan, CAO Dian-xue, FENG Jing, WU Rui-zhi, ZHANG Mi-lin. The electrochemical behaviors of Mg−8Li−0.5Y and Mg−8Li−1Y alloys in sodium chloride solution [J]. Journal of Power Sources, 2013, 239: 265−268.

[24] WANG Nai-guang, WANG Ri-chu, FENG Yan, XIONG Wen-hui, ZHANG Jun-chang, DENG Min. Discharge and corrosion behaviour of Mg−Li−Al−Ce−Y−Zn alloy as the anode for Mg−air battery [J]. Corrosion Science, 2016, 112: 13−24.

[25] YUASA M, HUANG Xin-sheng, SUZUKI K, MABUCHI M, CHINO Y. Discharge properties of Mg−Al−Mn−Ca and Mg−Al−Mn alloys as anode materials for primary magnesium−air batteries [J]. Journal of Power Sources, 2015, 297: 449−456.

[26] CHANG H W, QIU D, TAYLOR J A, EASTON M A, ZHANG M X. The role of Al2Y in grain refinement in Mg−Al−Y alloy system [J]. Journal of Magnesium Alloys, 2013, 1: 115−121.

[27] ZHANG Li, DENG Kun-kun, NIE Kai-bo, XU Fang-jun, SU Kun, LIANG Wei. Microstructures and mechanical properties of Mg−Al−Ca alloys affected by Ca/Al ratio [J]. Materials Science and Engineering A, 2015, 636: 279−288.

[28] SU Juan, GUO Feng, CAI Hui-sheng, LIU Liang. Study on alloying element distribution and compound structure of AZ61 magnesium alloy with yttrium [J]. Journal of Physics and Chemistry of Solids, 2019, 131: 125−130.
[29] YIM C D, KIM Y M, YOU B S, Effect of Ca addition on the corrosion resistance of gravity cast AZ31 magnesium alloy [J]. Materials Transactions, 2007, 48: 1023−1028.
[30] JIA Rui-ling, ZHANG Ming, ZHANG Li-na, ZHANG Wei, GUO Feng. Correlative change of corrosion behavior with the microstructure of AZ91 Mg alloy modified with Y additions [J]. Journal of Alloys and Compounds, 2015, 634: 263−271.
[31] WANG Lei, ZHANG Bo-ping, SHINOHARA T. Corrosion behavior of AZ91 magnesium alloy in dilute NaCl solutions [J]. Materials & Design, 2010, 31: 857−863.
[32] LI Chuan-qiang, TONG Zhi-pei, HE Yi-bin, HUANG Huai-pei, DONG Yong, ZHANG Peng. Comparison on corrosion resistance and surface film of pure Mg and Mg−14Li alloy [J]. Transactions of Nonferrous Metals Society of China, 2020, 30: 2413−2423.
[33] STERN M, GEARY A L, Electrochemical Polarization I. A theoretical analysis of the shape of polarization curves [J]. Journal of the Electrochemical Society, 1957, 104: 56−63.
[34] XU Shi-yuan, LIU Chu-ming, WAN Ying-chun, ZENG Guang, GAO Yong-hao, JIANG Shu-nong. Corrosion behaviour of Mg−Gd−Y−Zn−Ag alloy components with different sizes after cooling [J]. Transactions of Nonferrous Metals Society of China, 2021, 31: 1291−1302.
[35] BRAIL G, PÉBÈRE N. The corrosion of pure magnesium in aerated and deaerated sodium sulphate solutions [J]. Corrosion Science, 2001, 43: 471−484.
[36] DENG Min, WANG Lin-qian, HÖCHE D, LAMAKA S V, JIANG Ping-li, SNIHIROVA D, SCHARNAGL N, ZHELUDKEVICH M L. Ca/In micro alloying as a novel strategy to simultaneously enhance power and energy density of primary Mg−air batteries from anode aspect [J]. Journal of Power Sources, 2020, 472: 228528.
[37] SONG Yan, YANG Hua-bao, CHAI Yan-fu, WANG Qing-hang, JIANG Bin, WU Liang, ZOU Qin, HUANG Guang-sheng, PAN Fu-sheng, ATRENS A. Corrosion and discharge behavior of Mg−xLa alloys (x=0.0−0.8) as anode materials [J]. Transactions of Nonferrous Metals Society of China, 2021, 31: 1979−1992.
[38] GU Xiong-jie, CHENG Wei-li, CHENG Shi-ming, YU Hui, WANG Zhi-feng, WANG Hong-xia, WANG Li-fei. Discharge behavior of Mg−Sn−Zn−Ag alloys with different Sn contents as anodes for Mg−air batteries [J]. Journal of the Electrochemical Society, 2020, 167: 20501.
[39] YANG Hua-bao, WU Liang, JIANG Bin, LEI Bin, LIU Wen-jun, SONG Jiang-feng, HUANG Guang-sheng, ZHANG Ding-fei, PAN Fu-sheng. Effects of grain size on the corrosion and discharge behaviors of Mg−Y binary alloys for Mg−air batteries [J]. Journal of the Electrochemical Society, 2020, 167: 130515.
[40] WOO S K, BLAWERT C, YASAKAU K A, YI Sang-bong, SCHARNAGL N, SUH B, KIM Y M, YOU B S, YIM C D. Effects of combined addition of Ca and Y on the corrosion behaviours of die-cast AZ91D magnesium alloy [J]. Corrosion Science, 2020, 166: 108451.
[41] CHOI Y, KURODA K, OKIDO M. Temperature-dependent corrosion behaviour of flame-resistant, Ca-containing AZX911 and AMX602 Mg alloys [J]. Corrosion Science, 2016, 103: 181−188.
[42] DENG Min, WANG Lin-qian, HÖCHE D, LAMAKA S V, SNIHIROVA D, JIANG Ping-li, ZHELUDKEVICH M L. Corrosion and discharge properties of Ca/Ge micro-alloyed Mg anodes for primary aqueous Mg batteries [J]. Corrosion Science, 2020, 177: 108958.

钇和钙的添加对镁−空气电池阳极材料 AZ80 电化学行为和放电性能的影响

张钰雯茜[1]，韩 璐[1]，任凌宝[2]，范玲玲[1]，郭阳阳[3]，周明扬[4]，权高峰[1]

1. 西南交通大学 材料科学与工程学院 材料先进技术教育部重点实验室，成都 610031；
2. 西安交通大学 金属材料强度国家重点实验室 微纳尺度材料行为研究中心，西安 710049；
3. 西安稀有金属材料研究院有限公司，西安 710049；
4. 中国核动力研究设计院 核反应堆系统设计技术重点实验室，成都 610213

摘 要：研究钇(Y)、钇+钙(Y+Ca)的添加对镁−空气电池阳极材料 Mg−8Al−0.5Zn−0.2Mn(AZ80)合金电化学行为和放电性能的影响。结果表明，添加 0.2%(质量分数)的 Y 可以提高 AZ80 阳极的耐腐蚀性和放电活性。这是因为在 AZ80+0.2Y 合金基体中分布着细小弥散的球形 β-$Mg_{17}Al_{12}$ 相，可以抑制严重的局部腐蚀和“块状效应”，还有利于 α-Mg 的快速活化。同时添加 0.2% Y 和 0.15% Ca(质量分数)会使晶粒细化、β-$Mg_{17}Al_{12}$ 相减少，导致放电电压进一步提高。然而，AZ80+0.2Y+0.15Ca 阳极的耐蚀性和阳极效率却不如 AZ80+0.2Y，这主要与 $Mg_{17}Al_{12}$ 和 Al_2Y 化合物中掺杂了 Ca 有关。因此，AZ80+0.2Y 阳极表现出优异的综合放电性能，在电流密度为 80 mA/cm^2 时，其放电容量和阳极效率最高，分别为 1525 mA·h·g^{-1} 和 67%，比 AZ80 合金阳极的分别提高 13%和 14%。

关键词：镁−空气电池；Mg−Al−Zn 阳极；放电性能；电化学行为

(Edited by Bing YANG)